

# **A Method to Assess the Surface Urban Heat Island Effect Using Hemispherical Radiometric Surface Temperatures**

by

Michael A. Allen

A thesis  
presented to the University of Western Ontario  
in fulfillment of the  
thesis requirement for the degree of  
Master of Science

London, Ontario, Canada, 2017

© Michael A. Allen 2017

I hereby declare that I am the sole author of this thesis. This is a true copy of the thesis, including any required final revisions, as accepted by my examiners.

I understand that my thesis may be made electronically available to the public.

## **Abstract**

This is the abstract.

## **Acknowledgements**

These are my Acknowledgments

# Table of Contents

<b>List of Tables</b>	<b>vii</b>
<b>List of Figures</b>	<b>viii</b>
<b>Glossary</b>	<b>ix</b>
<b>1 Introduction</b>	<b>1</b>
1.1 Defining the urban surface . . . . .	1
1.2 The urban radiation budget . . . . .	1
1.3 The structure of the following sections . . . . .	1
<b>2 A method to correct upwelling longwave radiation to estimate hemispherical urban surface temperature</b>	<b>2</b>
2.1 Introduction . . . . .	2
2.2 Atmospheric effects on TIR . . . . .	4
2.2.1 Relating TIR and surface temperature . . . . .	6

2.2.2	Atmospheric correction of near-ground TIR . . . . .	8
2.3	A "rolling lookup table" method for hemispherical atmospheric correction . . . .	11
2.3.1	Study area . . . . .	12
2.3.2	Modeling path lengths of 3-dimensional terrain . . . . .	14
2.3.3	Modeling hemispherical irradiances . . . . .	15
2.4	Evaluation of the method using profiles of upwelling longwave radiation over a homogenous planar surface . . . . .	17
<b>3</b>	<b>A climatology of urban surface heat islands derived from hemispherical radiometric surface temperatures</b>	<b>19</b>
3.1	Introduction . . . . .	19
3.2	Bias in Thermal remote sensing . . . . .	21
	<b>References</b>	<b>24</b>

# List of Tables

2.1	Weightings to produce $T'_{\text{rad}}$ for different geometric representations of the Basel street canyon. . . . .	14
-----	---	----



# List of Figures

2.1	Spectral transmission of water vapor as a function of height. Black and grey shading indicate opaque (0% transmittance) and transparent (100% transmittance) bands respectively. Redo this figure with wavelength and colorbar? . . . . .	5
2.2	Variable path geometry inherent with wide-FOV near-ground sensor visualized over an idealized 2-dimensional urban area. . . . .	10
2.3	A workflow schematic depicting the input, model, and output-processing steps of a "rolling lookup table method" for hemispherical radiometric surface temperature retrieval. . . . .	12
2.4	A typical 2-dimensional (b) radiative transfer schematic adapted for an idealized 3-dimensional urban area (a). In 3-dimensions, path length for a given zenith angle can change significantly with azimuth angle. Dotted lines indicate the potential for absorption by the intervening atmospheric layer . . . . .	16

# Glossary

**atmospheric window** A region of the electromagnetic spectrum over which the atmosphere is transmissive. Two are located in the thermal infrared [waveband](#) at approximately 3–5 and 8—14 $\mu\text{m}$ . [4](#)

**boundary-layer** description [3](#)

**field-of-view** description [9](#)

**pyrgeometer** description [3](#)

**urban heat island effect** The tendency for cities to store and emit a greater amount of heat compared to non—urbanized surroundings. Generally manifests in elevated urban air and surface temperatures. [3](#)

**waveband** The range of wavelengths in between upper and lower bounds. Usually refers to the spectral range over which a sensor responds. [ix](#), [4](#)

# **Chapter 1**

## **Introduction**

### **1.1 Defining the urban surface**

Sometimes I have no idea what I am doing.

### **1.2 The urban radiation budget**

### **1.3 The structure of the following sections**

# Chapter 2

## A method to correct upwelling longwave radiation to estimate hemispherical urban surface temperature

### 2.1 Introduction

Thermal infrared (TIR) remote sensing of land surface temperature ( $T_{\text{surf}}$ ) has emerged as a primary research focus in climatology, as researchers seek to better describe spatiotemporal patterns of  $T_{\text{surf}}$  globally and better understand how anthropogenic modification of earth's surface influences land  $T_{\text{surf}}$  with links to the climate at-large. Over the last two decades, use of thermal remote sensing of surface climates has expanded significantly — both in terms of the volume and breadth of remote sensed study and its explicative importance in climatology as a discipline. Thermal remote sensing of earth's surface has applications over a wide range of disciplines: from informing micro-, urban-, and global-scale climate models, to aiding decision

making and mitigation praxis with respect to climate change and the [urban heat island effect](#).

Within urban climatology, a combination of satellite, aerial, and ground-based thermal remote sensors have been integral in elucidating the spatial [14], temporal [11], and geometric [19] effects of the built environment on land  $T_{\text{surf}}$ ; in evaluating and partitioning urban surface energy balances [2, 23] and; in characterizations of the relationship between surface and [boundary-layer](#) air temperatures ( $T_{\text{air}}$ ) [18]. These advances have been aided by substantial improvements in sensor ground, spectral, and radiometric resolutions, and by the proliferation of both large-scale public satellite remote sensing campaigns and low-cost aerial and near-ground thermography. However, in spite of its widespread usage, several questions concerning the use and validity of urban remote thermal remote sensing, first posed in Roth et al. 1989 [14], have yet to be sufficiently answered, viz,

1. What is the nature of the surface 'seen' by a thermal remote sensor?
2. How does  $T_{\text{surf}}$  observed by a remote sensor relate to the 'true' temperature governing the surface-atmosphere interface?

In this paper, we seek to examine question two by introducing and evaluating a method for atmospheric and emissivity correction of near-ground hemispherical TIR — measured via [pyrgeometer](#) — for hemispherical radiometric temperature ( $T_{\text{hem}}$ ) retrieval. These measures are common to most urban energy balance assessments and thus constitute a hitherto untapped method for urban  $T_{\text{surf}}$  analysis. A companion paper responds to question one through an analysis of a climatology of  $T_{\text{hem}}$  and derived surface UHI (sUHI), to quantify geometric and temporal biases across multiple methods for remote sensing of urban  $T_{\text{surf}}$ .

## 2.2 Atmospheric effects on TIR

Although most thermal remote sensors operate within one of the [atmospheric windows](#) — where atmospheric effects are greatly reduced — virtually any remote sensed TIR signal is subject to radiative effects from the intervening atmosphere between the surface and the sensor. Over much of the thermal infrared [waveband](#) the atmosphere emits radiation and absorbs a fraction of radiation emitted by the surface. In addition, the earth (and indeed the urban surface) reflects a portion of incoming solar radiation. Thus, a TIR signal measured from a remote sensing platform is almost certainly not equal to the ground emitted signal. These effects can lead to differences between the 'true' radiometric  $T_{\text{surf}}$  and the remote sensed  $T_{\text{surf}}$  of over 10 K for satellite platforms [\[5\]](#) and over 6 K for near-ground sensors [\[7\]](#). Moreover, because atmospheric and emissivity effects are a function of non-uniform and spatiotemporally variant surface and atmospheric properties, their associated errors change depending on instrument type, study location, and ambient conditions. As intersite and time-sequential analysis is a significant goal of most thermal remote sensed studies (urban or otherwise) these effects cannot be ignored.

Spectral transmission of longwave radiation through a given layer of atmosphere varies significantly based on wavelength, path geometry, and column absorber content (primarily  $\text{H}_2\text{O}$ ,  $\text{CO}_2$ , and to a lesser extent  $\text{O}_3$ ,  $\text{N}_2\text{O}$ ,  $\text{CO}$ ,  $\text{CH}_4$ , and  $\text{O}_2$  [\[8\]](#)). Variation in band-by-band longwave transmittance with path length is greatest at urban scales (approximately 1 to 50 meters), where transparent spectral bands can quickly become opaque with small changes in path length or absorber content - illustrated in figure [2.1](#). Thus, transmittance of TIR near the surface is highly dependent on surface-sensor-sun geometry, instrument properties, and synoptic conditions. Indeed, accurate assessment of atmospheric influence on TIR may be most complex when measured near the surface.

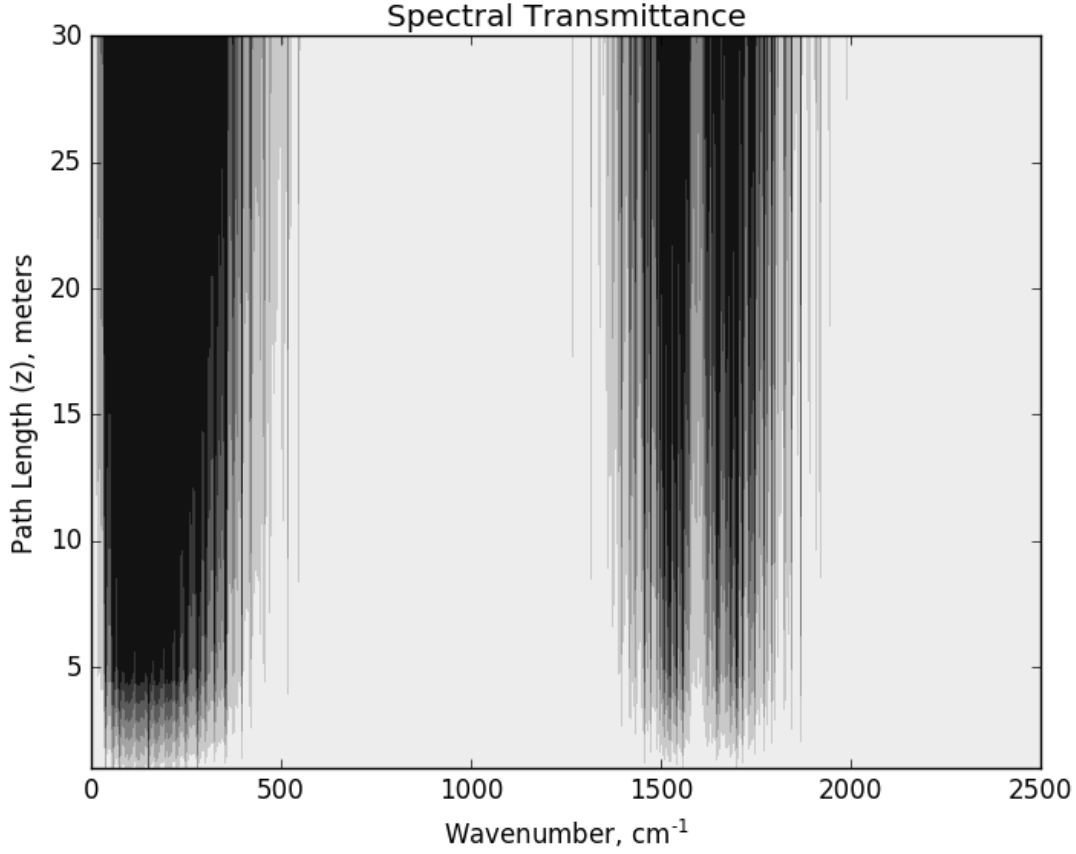


Figure 2.1: Spectral transmission of water vapor as a function of height. Black and grey shading indicate opaque (0% transmittance) and transparent (100% transmittance) bands respectively. Redo this figure with wavelength and colorbar?

The radiation passing through a layer of atmosphere from an emitting surface can be described in a number of ways. *Spectral directional radiance*  $R(\lambda)$ , at height  $z$  and from a direction defined by zenith angle  $\theta$ , and azimuth angle  $\phi$  is commonly written as

$$R_z^\uparrow(\lambda, \theta, \phi) = \tau_\lambda \epsilon R_0^\uparrow(\lambda) + (1 - \epsilon) R_{sky}^\downarrow(\lambda) + (1 - \tau_\lambda) R_{atm}^\uparrow(\lambda) \quad (2.1)$$

where  $\epsilon$  is surface emissivity,  $\tau_\lambda$  is spectral "slab" transmittance through the layer between the emitting surface ( $z = 0$ ) and  $z$ . The same spectral TIR signal, as measured by a narrow-FOV sensor mounted at height  $z$ , passes through an instrument shield (or dome) with spectral transmittance  $\tau_d$ , and is integrated over the sensor waveband (bounded by  $\lambda_1$  and  $\lambda_2$ ) to yield a *directional radiance*  $L'$  as 'seen' by the sensor

$$L'_z(\theta, \phi) = \int_{\lambda_1}^{\lambda_2} \tau_d(\lambda) R_z^\uparrow(\lambda) d\lambda \quad (2.2)$$

which, integrated over the hemisphere with respect to zenith  $\theta$  angle and azimuth  $\phi$  angle, yields an *irradiance*  $L$  at height  $z$ ,

$$L_z = \int_0^{2\pi} \int_0^{\pi/2} L'_z(\theta, \phi) \cos \theta \sin \theta d\theta d\phi \quad (2.3)$$

### 2.2.1 Relating TIR and surface temperature

TIR received by a remote sensor can be related to the emitting body's temperature in a number of ways — each producing different conceptions of  $T_{\text{surf}}$  from different instrument and sensor types. As such, the term "surface temperature" with respect to a remote sensed TIR is vague and can refer to several definitions of "surface" and "temperature". Thus, proper terminology must be attached to land  $T_{\text{surf}}$  inferred from TIR. Definitions and nomenclature conventions for multiple methods for  $T_{\text{surf}}$  retrieval are discussed at length in Norman & Becker, (1995)[10].

Directional radiance  $L'_z$  detected from a narrow-FOV sensor operating over waveband ( $\lambda_1$  —  $\lambda_2$ ) and viewing the surface from some orientation described by  $\theta, \phi$  can be used to infer a *directional brightness temperature*  $T'_{\text{bright}}(\theta, \phi)$  via an inversion of the Planck function



multiplied by normalized sensor response integrated over the sensor waveband,

$$L'_z(T'_{bright}(\theta, \phi)) = \int_{\lambda_1}^{\lambda_2} \frac{f(\lambda)C_1}{\pi \lambda^5 \left( \exp \left( \frac{C_2}{\lambda T'_{bright}(\theta, \phi)} \right) \right)} d\lambda \quad (2.4)$$

where  $C_1 = 3.7404 \cdot 10^8 \text{ W}\mu^4\text{m}^{-2}$ ,  $C_2 = 14387\mu\text{K}$ , and relative sensor response  $r(\lambda)$  normalized via,

$$1 = \int_{\lambda_1}^{\lambda_2} r(\lambda) d\lambda \quad (2.5)$$

Similarly irradiance  $L_z$  received by a broadband hemispherical sensor (such as a pyrgeometer), can be used to infer a *hemispherical brightness temperature*  $T_{\text{bright}}$  through an inversion of the Stefan-Boltzmann law,

$$L_z = \bar{r}(\sigma T_{\text{bright}}^4) \quad (2.6)$$

where  $\sigma$  is the Stefan-Boltzmann constant and  $\bar{r}$  is Planck weighted average broadband sensor response computed as,

$$\bar{r} = \frac{\int R(\lambda) r(\lambda) d\lambda}{\int R(\lambda) d\lambda} \quad (2.7)$$

with  $R(\lambda)$  computed from a Planck function at an approximated  $T_{\text{bright}}$ .

In addition, a simple approximation of  $T_{\text{bright}}$  can be inferred from directional radiance using equation 2.6 by replacing  $L_z$  with  $L'_z$  multiplied by a constant. This method is commonly

used to infer  $T_{\text{bright}}$  from infrared thermometers (IRT) operating over the atmospheric window (where atmospheric correction magnitudes are small and  $T_{\text{bright}}$  is a reasonably accurate approximation of  $T_{\text{surf}}$ ). However, constants must be calibrated for the range of expected  $T_{\text{surf}}$  as the relationship between  $L_z$  and  $L'_z$  is not perfectly linear.

Inversions of uncorrected directional radiances or irradiances using the Planck function or the Stefan-Boltzmann law yield a temperature equal to that of a blackbody emitting the same amount of radiation as detected by the sensor. Since  $L_z$  is unlikely to be equal to  $L_0$ ,  $T_{\text{bright}, 0}$  and  $T_{\text{bright}, z}$  often show significant variation based on sensor characteristics, ambient conditions, and surface-sensor geometry. Hence, remote sensed  $T_{\text{bright}}$  is generally considered only a rough approximation representation of kinetic or thermodynamic  $T_{\text{surf}}$ .

To retrieve a more accurate estimation of the 'true'  $T_{\text{surf}}$ , the same inversions can be applied to TIR measurements after correction for atmospheric and surface emissivity effects (e.g. transformations of the TIR signal to represent that at  $z = 0$  if the surface was emitting as a perfect blackbody) to yield a direction radiometric surface temperature  $T_{\text{rad}}$  for atmospheric and emissivity corrected directional radiances, a hemispherical radiometric surface temperature  $T_{\text{hem}}$  for atmospheric and emissivity corrected irradiances.  $T_{\text{rad}}(\theta, \phi)$  and  $T_{\text{hem}}$  provide a better approximation of the true  $T_{\text{surf}}$  by representing the temperature at which the surface is radiating integrated over the sensor FOV.

### 2.2.2 Atmospheric correction of near-ground TIR

A large number of correction routines have been developed to remove atmospheric and emissivity effects from aerial and satellite TIR signals and derive accurate  $T_{\text{rad}}$ . Methods range from simple mono- [12] and split-window [22] routines for single- and multi-channel remote sensors to schemes that integrate a radiative transfer code to isolate the surface emitted signal

from interfering signals. Boundary conditions are standard across most correction methods: often requiring vertical profiles of  $T_{\text{air}}$ , humidity, pressure, and aerosol content to remove atmospheric effects, and assessments of surface radiative properties to correct for emissivity effects. However, correction methods are generally instrument (or at least platform) specific and difficult to generalize across sensor and platform types. Few methods exist for correction of ground based remote sensed TIR — none of which are robust enough to correct irradiances upwelling from rough terrain measured wide-field-of-view(FOV) sensor. In part, this is due to the fact that near ground thermal sensors have only recently become sensitive enough to require correction. However, a new breed of more accurate radiometers and thermal imagers should prompt a critical reevaluation of this assumption.

Atmospheric correction of near-ground remote sensed TIR is subject to a unique set of challenges compared to satellite and aerial platforms. Near-ground remote sensors have complex, multiple line-of-sight (LOS) geometry - illustrated in figure 2.1 for a wide-FOV instrument. Surface to sensor path lengths vary significantly over the sensor FOV, even when measured close (less than 5m) above the surface. This creates the potential for non-uniform atmospheric effects over the sensor FOV and necessitates a multi-LOS correction to retrieve accurate  $T_{\text{rad}}$ . The addition of 3-dimensional surface geometry further amplifies this effect, as some paths may intersect with raised vertical, sloped, and horizontal features. In effect, with near-ground wide-FOV sensors, surface geometry is non-trivial and must be represented in atmospheric correction routines. In contrast, over a scene retrieved via satellite, spatial variability in surface geometry and LOS angle have a negligible effect on path length. Atmospheric correction routines for satellite retrieved TIR, therefore, assume uniform or single-LOS geometry because the TIR signal passes through a relatively constant volume of atmosphere over the projected sensor FOV, regardless of surface geometry. This greatly reduces the complexity of correction routines for satellite or aerial thermography.

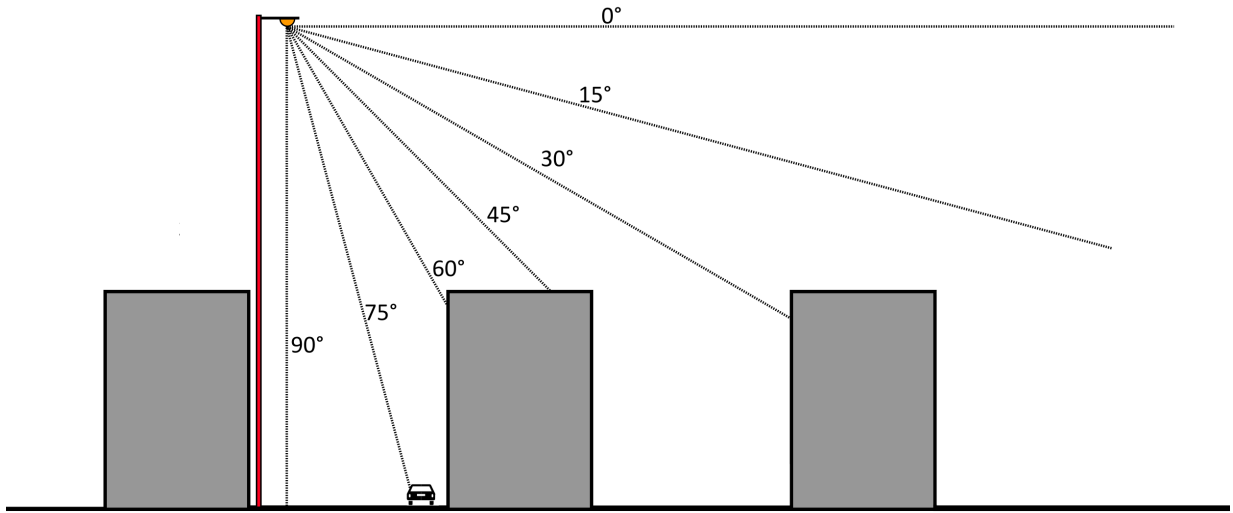


Figure 2.2: Variable path geometry inherent with wide-FOV near-ground sensor visualized over an idealized 2-dimensional urban area.

Several multi-LOS atmospheric correction routines have been developed for near-ground TIR: Meier et al., 2011 describes a correction method for oblique angled urban thermography [7]. Path lengths were calculated for each pixel over the FOV of a tower-mounted thermal imager angled obliquely toward the urban surface. A correction factor was then computed and applied using a radiative transfer code initialized using isothermal, isohumal atmospheric profiles for each time step. Applied over a time-series of images, the result is a continuous atmospherically corrected series of thermal images with each pixel representing a different  $T_{\text{rad}}$ . However, the method uses visual-band images and a GIS database to represent urban geometry for each pixel's LOS - a technique not possible with a pyrgeometer, which returns a single integrated irradiance at each time-step. Moreover, the target instrument operates over a narrow waveband, reducing the magnitude and variance in atmospheric transmission over the sensor response curve. Thus, the method is not directly generalizable to correction TIR as measured via pyrgeometer. Kotani & Sugita, 2009 describes a method for correction of wide-FOV

(pyrgeometer) TIR Irradiances [6] over planar terrain. However, these methods are limited to narrow-FOV thermal imagers and sensors over planar surfaces respectively. A method which combines Meier et al., 2009’s representation of complex surface geometry and Kotani & Sugita, 2009’s broadband hemispherical integration is needed for atmospheric correction of urban TIR measured from a downward facing pyrgeometer. A method to correct hemispherical broadband TIR as measured from a downward facing pyrgeometer needs to combine the two for accurate  $T_{\text{hem}}$  retrieval over rough terrain.

## **2.3 A ”rolling lookup table” method for hemispherical atmospheric correction**

The ”rolling lookup-table” method described in this study uses a sensor view model in conjunction with a radiative transfer code to model hemispherical irradiances upwelling from a simplified isothermal 3-dimensional representation of the target study area. In summary, the method (depicted in figure 2.3) uses vertical profiles of measured  $T_{\text{air}}$  and humidity to model at-sensor spectral radiances at  $5^\circ$  increments over the sensor FOV for a predefined range of possible  $T_{\text{hem}}$  at each time-step. Spectral directional radiances are convolved by a dome transmittance curve, integrated over the sensor waveband, and weighted for their respective angular view factor. Weighted directional radiances are then integrated over the hemisphere and aggregated into a lookup table (LUT) of modeled irradiance— $T_{\text{hem}}$  pairings for each timestep, unique to the vertical profile of measured  $T_{\text{air}}$  and humidity. Finally, for each time-step, measured irradiances are matched with the closest modeled irradiances in the associated LUT to return an atmospherically corrected hemispherical surface temperature ( $T_{\text{hem}}$ ). This process is repeated at 30 minute intervals to yield a continuous climatology of urban  $T_{\text{hem}}$  for surface

urban heat island (sUHI) analysis. The following sections introduce the study area and describe the sensor view modeling, radiative transfer, and post-processing steps of the method.

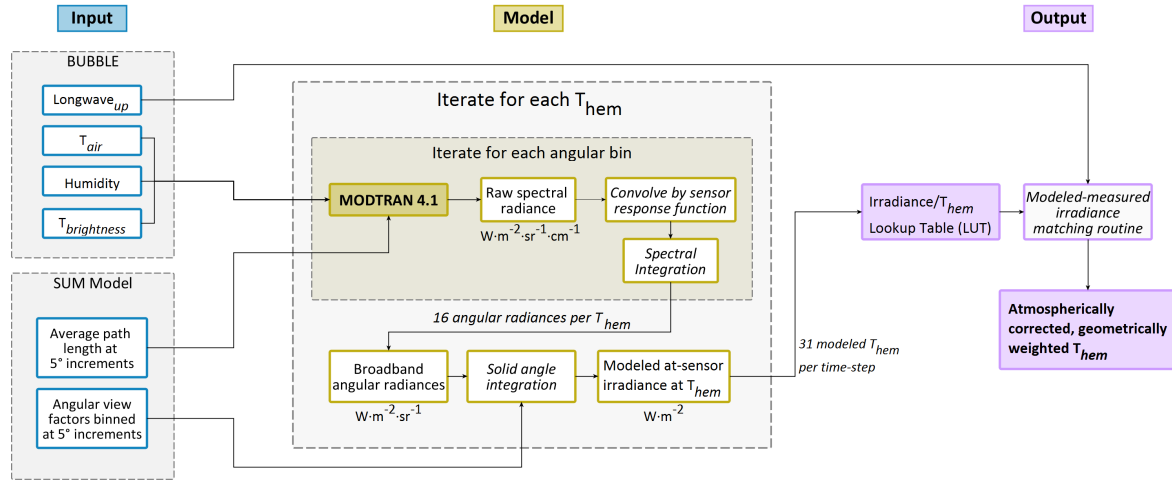


Figure 2.3: A workflow schematic depicting the input, model, and output-processing steps of a "rolling lookup table method" for hemispherical radiometric surface temperature retrieval.

### 2.3.1 Study area

As discussed in Section 2.2.2, atmospheric correction of longwave irradiances measured from downward-facing, near-ground, wide-FOV sensors must account for surface geometry - particularly when mounted to view complex surface geometry. Hence, routines to retrieve atmospherically corrected urban T<sub>hem</sub> from upwelling longwave irradiances are inherently site specific. However, it is important to note that although correction magnitudes described in this paper are not generalizable, the correction method described in this paper can readily be adapted to different study sites, pyrgeometer types, and unique surface geometries.

With methodological generalizability in mind, a "rolling lookup table" atmospheric correction method was developed to retrieve radiometric  $T_{\text{hem}}$  for a climatology of upwelling longwave irradiances measured from above the Sperrstrasse urban street canyon in Basel, Switzerland. The site, instrumented as a part of the Basel Urban Boundary Layer Experiment (BUBBLE) [13], has an approximately northeast-southwest orientation and site morphology representative of local climate zone (LCZ) 2<sup>1</sup> [17]. LCZ classification was based on an assessment of surface characteristics in a 250m circular area extending from the Sperrstrasse tower using a 1m raster digital building model (DBM). Thus, the morphological parameters identified in [13] are representative of the vast majority of the pyrgeometer footprint. However, it should be noted that vegetation was not included in the DBM, and thus is not represented in morphological assessment or the sensor view model.

For the nine month period between November 2001 and July 2002, a triangular lattice tower was installed skewed towards the southeast facing wall near the center of the Sperrstrasse canyon to observe a full suite of meteorological, radiation, and flux parameters. Profiles of  $T_{\text{air}}$  and humidity were measured from seven heights extending from 2.5m to 31.5m above the canyon floor (with the highest observation level at approximately 2.17 times mean building height). Upwelling and downwelling short/longwave fluxes were measured at the lowest and highest tower heights, with an additional downward facing pyrgeometer mounted at roof level in the center of the canyon. In addition, during a summertime intense operation period (IOP) an array of narrow-FOV IRTs was installed to view individual facet surface temperatures ( $T_{\text{facet}}$ ) of approximately the same urban patch viewed by the pyrgeometer.

The BUBBLE Sperrstrasse site was chosen for two primary reasons: 1. The study site provided a long-term climatology of radiation and meteorological variables for a representative

---

<sup>1</sup>Site surroundings can be described by the following morphological parameters: mean building height: 14.6m, plan aspect ratio: 0.54, complete aspect ratio: 1.92, local canyon aspect ratio: 1.0, and average shortwave albedo: 0.11 [13].

mid-latitude city over a diverse range of synoptic conditions. This allowed for examination of urban  $T_{\text{surf}}$ , atmospheric correction magnitudes, and sUHI magnitudes over a wide range of mid-latitude conditions. 2.  $T_{\text{facet}}$  measured during the summertime IOP allowed for direct climatological comparison of  $T_{\text{hem}}$  to wall ( $T_{\text{wall}}$ ), roof ( $T_{\text{roof}}$ ), and road ( $T_{\text{road}}$ ) surface temperatures of both the northwest- and southeast-facing sides of the canyon. In addition, several hypothetical sensor views of the canyon were simulated by weighting to represent different geometric representations of the canyon, including a nadir/plan view, an oblique south-facing, and an oblique north-fac from narrow-FOV sensors and a complete, 3-dimensional view of the canyon. This facilitated comparison of  $T_{\text{hem}}$  against different instrument types and platforms to identify and quantify biases in each method. In each representation, different weightings were applied to  $T_{\text{wall}}$ ,  $T_{\text{roof}}$ , and  $T_{\text{road}}$  on both sides of the canyon to represent different sensor orientations and sampling regimes. Weightings for each representation are described in table 2.1.

Table 2.1: Weightings to produce  $T'_{\text{rad}}$  for different geometric representations of the Basel street canyon.

	Road	Northwest Roof	Southeast Roof	Northwest Wall	Southeast Wall
Complete	0.33	0.16	0.16	0.16	0.16
Nadir	0.46	0.27	0.27	0.00	0.00
Oblique (south-facing)	0.20	0.25	0.25	0.00	0.30
Oblique (north-facing)	0.20	0.25	0.25	0.30	0.00

### 2.3.2 Modeling path lengths of 3-dimensional terrain

Radiative transfer of broadband longwave radiation is highly dependent on sensor-surface geometry. To calculate surface-sensor path lengths, the Surface-Sensor-Sun



Urban Model ( $S^3UM$ ) [15] is initialized with a simplified, orthogonal 3-dimensional DBM representing the area immediately surrounding the sensor. In  $S^3UM$ , urban features (roads, roofs, buildings, etc.) are constructed from an array of horizontal and stacked vertical patches (representing rooftops/roads and walls respectively). After indicating sensor FOV and position over the DBM, the model determines which patches have an unobstructed line of sight to the sensor and calculates the path distance from "seen" patches to the sensor. Path lengths are binned at  $5^\circ$  increments from the nadir and averaged to return an azimuthally averaged path length for each  $5^\circ$  bin. Using azimuthally averaged path lengths in lieu of a full 3-dimensional radiative transfer model significantly reduces the computational time required to model each irradiance- $T_{hem}$  pairing, as at-sensor radiance can be computed independent of azimuth angle. Radiative transfer is thus reduced to a two dimensional problem (shown in panel (b) of figure 2.3.2) in which an azimuthally averaged radiance is simulated for each zenith angle. The view factors required to weight directional radiances in the hemispherical integrated are computed. While generating azimuthally averaged path lengths,  $S^3UM$  calculates view factors for each solid angle bin used in weighting 2-dimensional angular radiances during the hemispherical integration. By using azimuthally averaged path lengths in lieu of However, because hemispherical TIR sensor returns a bulk irradiance, the sensor signal does not need to be computed for each point of the

### 2.3.3 Modeling hemispherical irradiances

With path length geometries calculates in  $S^3UM$ , MODTRAN 4.1 is initialized with 30-minute averaged profiles of  $T_{air}$  and humidity to model at-sensor spectral directional radiances over a waveband of  $0-2500\text{cm}^{-1}$ . Aerosol and above canyon meteorological conditions are informed by the Mid-Latitude Summer standard atmosphere when daytime

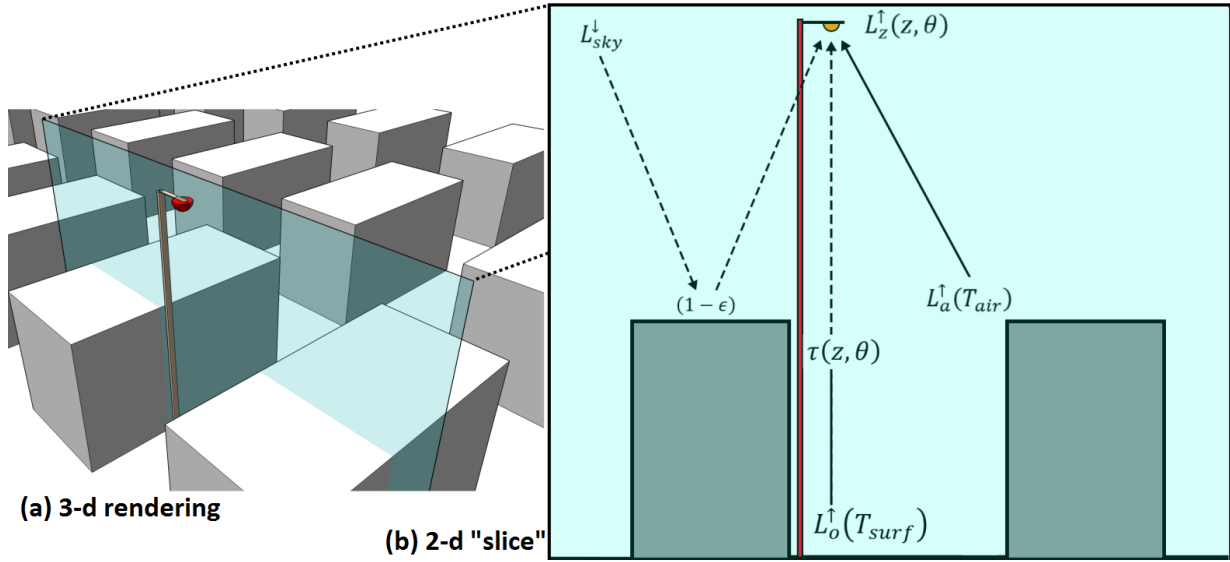


Figure 2.4: A typical 2-dimensional (b) radiative transfer schematic adapted for an idealized 3-dimensional urban area (a). In 3-dimensions, path length for a given zenith angle can change significantly with azimuth angle. Dotted lines indicate the potential for absorption by the intervening atmospheric layer

maximum  $T_{air}$  is greater than  $10^\circ$ . For days with daytime  $T_{air}$  maximum below  $10^\circ$ , the Mid-Latitude Winter standard atmosphere is substituted. In spite of significant computational efficiency gains from reducing 3-dimensional radiative transfer to azimuthally averaged 2-dimensions, the method still requires significant computational time to write input cards and model spectral radiances - in this case, with a path length increment of 5 and a LUT of 31 modeled irradiance— $T_{hem}$  pairings, each time-step requires 496 independent MODTRAN runs

## 2.4 Evaluation of the method using profiles of upwelling longwave radiation over a homogenous planar surface

MODTRAN has been shown to effectively model near-ground radiative transfer at urban-scale path lengths in 2-dimensions. However, the method detailed in this paper includes significant post-processing to collate point-to-point radiances into 3-dimensional hemispherical irradiances. In addition, the method accounts for site-specific surface geometry, which has a significant influence on boundary-layer transmittance of broadband longwave radiation. Thus, prior to deriving a climatology of radiometric urban  $T_{\text{em}}$ , the method was evaluated over a simple surface with known surface characteristics. Thus, divergences are solely the result of differential atmospheric effects with increasing height above ground, which should be accounted for by the model. It is assumed that each pyrgeometer in this validation views a patch with approximately the same temperature.

Profiles of upwelling longwave radiation, downwelling shortwave, air temperature, and humidity at 2m, 10m, and 30m were obtained from the Payerne station, located 50 miles southwest of Basel, Switzerland in a cultivated field. To evaluate the method, we used a modified version of the workflow described in XXXX. Brightness temperature calculated from the lowest upwelling longwave measurement was used to model irradiances at 10m and 30m at each time-step. Downwelling shortwave radiation was used to categorize test days based on cloud cover. The daytime air temperature profile was modified to replicate typical lapse rates in the Sperrstrasse canyon. Unlike, Kotani & Sugita (2009), an isothermal atmospheric profile was not sufficient to accurately model upwelling longwave divergences (nor fluxes) of planar terrain. Although thermal stratification is likely to be relatively small by day in an urban canyon [9] — where strong microscale contrasts in  $T_{\text{surf}}$  foster canyon mixing and neutral stability — the large daytime  $T_{\text{surf}} - T_{\text{air}}$  differential and the path-length/transmittance gradient can create large

positive divergences ( $5-15 \text{ Wm}^{-2}$ , CHECK THIS). As such, we suggest using a full canyon  $T_{\text{air}}$  /humidity profile to

Modeled upwelling longwave at 10m and 30m and divergences are compared to their measured counterparts in figure a. Both fluxes and divergence show strong correlations, thus we conclude: 1. Irradiances measured at 2m are free from significant atmospheric influence as an uncorrected irradiance provided an accurate  $T_{\text{surf}}$  for modeling of 10m and 30m Irradiances As such, brightness  $T_{\text{em}}$  and radiometric  $T_{\text{em}}$  are approximately equal when  $z \leq 2\text{m}$ . Although, it should be noted that a 2m sensor is not representative of canyon geometry and should not be used to derive urban  $T_{\text{em}}$ . 2. The method is sensitive enough to model divergences in a large layer above a flat surface. Urban divergences are likely to be smaller with less frequent and less severe stable stratifications. Thus, we can safely make the assumption that the method is effective over complex terrain provided path length geometries are accurately replicated in SUM.

## **Chapter 3**

# **A climatology of urban surface heat islands derived from hemispherical radiometric surface temperatures**

### **3.1 Introduction**

The temperature of the surface is integral in understanding, predicting, and modeling boundary-layer air temperature patterns, surface energy balances, and, in urban areas, has important implications for human thermal comfort and building energy usage. Urban modification of surface geometry and thermal, radiative, moisture, and aerodynamic properties results in differential surface heating and cooling patterns and strong microscale spatiotemporal variations in urban surface temperature. Integrated up to larger scales, urban areas tend to store and generate more heat relative to non-built surroundings and, as a result, are generally warmer — a phenomenon termed the urban heat island effect (UHI). As such, accurate, spatiotemporally

continuous and geometrically representative characterization of surface temperatures has long been a goal in urban climatology. The proliferation of satellite and aerial thermal infrared (TIR) remote sensing has enabled spatially-extensive, large-scale characterizations of surface climates at ever improving spatial and spectral resolutions. Such campaigns have elucidated urban surface temperature ( $T_{\text{surf}}$ ) and surface urban heat island (sUHI) patterns globally at large spatial scales. However, technological improvements in TIR remote sensing have yet to address a three potential sources of error when applied in urban areas:

1. Geometric undersampling of 3-dimensional terrain
2. Temporal discontinuity in overpass cycles and sensor sampling regimes
3. Clear-sky bias

These biases present a potentially significant source of error by failing to capture micro-scale temporal and geometric variations in urban  $T_{\text{surf}}$ .

Inter-site comparison is the crux of UHI analysis, thus it is imperative that urban surface temperature measurements are accurate and representative of coherent urban patches. Meta-analysis of air temperature UHI literature shows that these goals are not often not satisfied [16]. Given the relative difficulty in retrieving accurate, representative urban surface temperatures, similar conclusions are likely for sUHI analysis. In spite of this fact, and the short period over which large-scale generalizable methods for urban surface temperature acquisition have been available, study of sUHI has expanded significantly in the last twenty years [11, 21]. This paper presents a method to derive hemispherical radiometric urban  $T_{\text{surf}}$  ( $T_{\text{hem}}$ ) from hemispherical upwelling TIR as measured by inverted pyrgeometers. This method was developed to addresses biases inherent in traditional methods for urban  $T_{\text{surf}}$  retrieval by

providing temporally continuous, geometrically representative<sup>1</sup> urban  $T_{\text{surf}}$  under all-sky conditions for sUHI analysis. These measurements are often made as a part of the net radiation determination for urban energy balance studies.

### 3.2 Bias in Thermal remote sensing

Geometric biases in remote sensing of the urban surface are a result of its 3-dimensional, convoluted structure. Compared to flat terrain, complex urban surface geometry modifies receipt of incoming solar radiation and traps a portion of reflected solar and outgoing terrestrial radiation. Differential heating and shading patterns of vertical, sloped, and horizontal urban facets manifests in significant micro-scale contrasts in surface temperature. As such, measured radiometric surface temperature varies based on sensor field-of-view, viewing angle and direction, and sun-surface geometry this directional dependence of urban surface temperature is termed effective thermal anisotropy [20]. Traditional satellite or airborne remote sensing platforms, by viewing the surface in the nadir, sample only a fraction of the complete urban surface and fail to capture this effect leading to directional biases in measured urban surface temperature. Geometric undersampling by a remote sensor in the nadir manifests in an overestimation of daytime temperatures and underestimation of nighttime temperatures [1]. However, the magnitude and diurnal pattern of this bias is dependent on urban patch characteristics (canyon height-to-width ratio, canyon orientation and materials, vegetation coverage, etc.) and sensor viewing angle. Thus, parameterization schemes to account for urban effective anisotropy are difficult to generalize across urban sites, sensor types, and sensor orientations.

---

<sup>1</sup>Them is not perfectly representative of urban geometry. This is best illustrated by visualizing an urban area from the perspective of a downward facing fish-eye camera. However, it is undoubtedly more representative of urban geometry than most 2-dimensional views of the surface. This fact is discussed in more depth in sectionXXXX.

In addition to undersampling the urban surface, most thermal remote sensing platforms yield an instantaneous snap-shot and cannot characterize temporally continuous  $T_{\text{surf}}$  patterns. Temporal discontinuities in thermal remote sensing result in a number of sources of bias operating over a wide range of time scales. Aerial and satellite thermal remote sensing require clear sky conditions (clouds are opaque with respect to thermal infrared radiation). Hence, long term satellite characterizations of sUHI are biased towards conditions that maximize macro-scale urban-rural contrasts in surface temperature. This results in an overestimation of all-sky sUHI. Although

Over a day, sUHI is generally largest in the late afternoon, near solar noon, and just after sunset. Continuous sUHI analysis indicates that it exhibits a large diurnal amplitude. Satellite overpass cycles rarely coincide with sUHI maximums and are not standard across cities or platforms. Thus, analysis of sUHI patterns and magnitudes across cities and instrument platforms is difficult. High-frequency fluctuations in surface temperature add an additional and understudied bias to thermal remote sensing of urban surface temperature. Time series analysis of urban surface temperature shows significant microscale (second to minute) fluctuations in temperature [4]. Most thermal remote sensors observe surface temperatures instantaneously (rather than temporally averaged) and are potentially contaminated by microscale fluctuations. This is particularly salient in urban environments, where a large variety of fabric materials can produce significant directional contrasts in thermal admittance and thus spatial variations in the magnitude of microscale fluctuations depending on the facet material types viewed by the sensor. The effect of this phenomenon on thermal remote sensing has not been extensively studied, however, the magnitude of microscale fluctuations in surface temperature is significant relative to a typical sUHI signal and thus constitutes a potentially large source of bias.

Both geometric and temporal shortcomings limit the representativity of traditional remote sensed evaluations of urban  $T_{\text{surf}}$  and sUHI. The magnitude of these biases has not been



extensively studied in climatological form. This paper presents a method to both assess the magnitude of and overcome these biases.

# References

- [1] C. Adderley, A. Christen, and J. A. Voogt. The effect of radiometer placement and view on inferred directional and hemispheric radiometric temperatures of an urban canopy. *Atmospheric Measurement Techniques*, 8(2):1891–1933, 2015.
- [2] Bastiaanssen W.G.M., M. Meneti, R.A. Feddes, and a a M Holtslag. A remote sensing surface energy balance algorithm for land (SEBAL): Formulation. *Journal of Hydrology*, 212-213(JANUARY):198–212, 1998.
- [3] A Berk, L. S. Bernstein, and D. C. Robertson. MODTRAN: A Moderate Resolution Model for LOWTRAN7. Technical Report GL-TR-89-0122, 1989.
- [4] Andreas Christen, Fred Meier, and Dieter Scherer. High-frequency fluctuations of surface temperatures in an urban environment. *Theoretical and Applied Climatology*, 108(1-2):301–324, 2012.
- [5] D. I. Cooper and G. Asrar. Evaluating atmospheric correction models for retrieving surface temperatures from the AVHRR over a tallgrass prairie. *Remote Sensing of Environment*, 27(1):93–102, 1989.

- [6] Ayumi Kotani and Michiaki Sugita. Concise formulae for the atmospheric correction of hemispherical thermal radiation measured near the ground surface. *Water Resources Research*, 45(7):1–7, 2009.
- [7] F. Meier, D. Scherer, J. Richters, and A. Christen. Atmospheric correction of thermal-infrared imagery of the 3-D urban environment acquired in oblique viewing geometry. *Atmospheric Measurement Techniques*, 4(5):909–922, 2011.
- [8] F. Miskolczi and R. Guzzi. Effect of nonuniform spectral dome transmittance on the accuracy of infrared radiation measurements using shielded pyrrometers and pyrgeometers. *Applied Optics*, 32(18):3257, jun 1993.
- [9] Y. Nakamura and T. R. Oke. Wind, temperature and stability conditions in an east-west oriented urban canyon. *Atmospheric Environment (1967)*, 22(12):2691–2700, 1988.
- [10] John M. Norman and Francois Becker. Terminology in thermal infrared remote sensing of natural surfaces. *Agricultural and Forest Meteorology*, 77(3-4):153–166, 1995.
- [11] Shushi Peng, Shilong Piao, Philippe Ciais, Pierre Friedlingstein, Catherine Ottle, François Marie Bréon, Huijuan Nan, Liming Zhou, and Ranga B. Myneni. Surface urban heat island across 419 global big cities. *Environmental Science and Technology*, 46(2):696–703, 2012.
- [12] Z. Qin, A. Karnieli, and P. Berliner. A mono-window algorithm for retrieving land surface temperature from Landsat TM data and its application to the Israel-Egypt border region. *International Journal of Remote Sensing*, 22(18):3719–3746, 2001.
- [13] M. W. Rotach, Roland Vogt, C. Bernhofer, E. Batchvarova, A. Christen, A. Clappier, B. Feddersen, S.-E. Gryning, G. Martucci, H. Mayer, V. Mitev, Tim R. Oke, E. Parlow,

- H. Richner, M. Roth, Y.-A. Roulet, D. Ruffieux, J. A. Salmond, M. Schatzmann, and J. A. Voogt. BUBBLE an Urban Boundary Layer Meteorology Project. *Theoretical and Applied Climatology*, 81(3-4):231–261, 2005.
- [14] M. Roth, Tim R. Oke, and W. Emery. Satellite-derived urban heat islands from three coastal cities and the utilization of such data in urban climatology. *International Journal of Remote Sensing*, 10(11):1699–1720, 1989.
- [15] A. Soux, J. A. Voogt, and Tim R. Oke. A model to calculate what a remote sensor 'sees' of an urban surface. *Boundary-Layer Meteorology*, 111(1):109–132, 2004.
- [16] I. D. Stewart. A systematic review and scientific critique of methodology in modern urban heat island literature. *International Journal of Climatology*, 31(2):200–217, 2011.
- [17] Iain D. Stewart and Tim R. Oke. Local climate zones for urban temperature studies. *Bulletin of the American Meteorological Society*, 93(12):1879–1900, 2012.
- [18] Matthew J Stoll and Anthony J Brazel. Surface-air temperature relationship in the urban environment of Phoenix, Arizona. *Physical Geography*, 13(2):160–179, 1992.
- [19] J. A. Voogt and Tim R. Oke. Complete Urban Surface Temperatures. *Journal of Applied Meteorology*, 36(9):1117–1132, 1997.
- [20] J. A. Voogt and Tim R. Oke. Effects of urban surface geometry on remotely-sensed surface temperature. *International Journal of Remote Sensing*, 19(February 2015):895–920, 1998.
- [21] J. A. Voogt and Tim R. Oke. Thermal remote sensing of urban climates. *Remote Sensing of Environment*, 86(3):370–384, 2003.

- [22] Zhengming Wan and Jeff Dozier. A Generalized Split-Window Algorithm for Retrieving Land-Surface Temperature from Space. *IEEE Transactions of Geoscience and Remote Sensing*, 34(4):892–905, 1996.
- [23] Yasushi Yamaguchi and Soushi Kato. Analysis of urban heat-island effect using ASTER and ETM+ Data: Separation of anthropogenic heat discharge and natural heat radiation from sensible heat flux. *Remote Sensing of Environment*, 99:44–54, 2005.